Chemical Engineering Journal 496 (2024) 154081

Contents lists available at ScienceDirect

Chemical Engineering Journal

journal homepage: www.elsevier.com/locate/cej

Sub-minute carbonization of polymer/carbon nanotube films by microwave induction heating for ultrafast preparation of hard carbon anodes for sodium-ion batteries

Gyeongbeom Ryoo [a,b,1], Jiwon Shin [a,c,1], Byeong Guk Kim [a,d], Do Geun Lee [a,b], Joong Tark Han [a,d], Byeongho Park [e], Youngseok Oh [e], Seung Yol Jeong [a,d], Se-Hee Lee [c], Dong Yun Lee [b,*], Daeho Kim [a,*], Jong Hwan Park [a,d,*]

[a] Nano Hybrid Technology Research Center, Electrical Materials Research Division, Korea Electrotechnology Research Institute (KERI), Changwon 51543, Republic of Korea
[b] Department of Polymer Science and Engineering, Kyungpook National University, Daegu 41566, Republic of Korea
[c] School of Electronic and Electrical Engineering, Kyungpook National University, Daegu 41566, Republic of Korea
[d] Electric Energy & Material Engineering, KERI School, University of Science and Technology (UST), Changwon 51543, Republic of Korea
[e] Composites Research Division, Korea Institute of Materials Science (KIMS), Changwon 51508, Republic of Korea

ARTICLE INFO

Keywords:
Sodium-ion batteries
Hard carbon anodes
Ultrafast microwave induction heating
Carboxymethyl cellulose
Single-walled carbon nanotubes

ABSTRACT

Hard carbons (HCs) are excellent anode materials for sodium-ion batteries (SIBs). However, the carbonization and granulation of HC powders involve complex processes and require considerable energy. Here, we developed a facile method for manufacturing HC anodes for SIBs via a novel microwave induction heating (MIH) process for polymer/single-walled carbon nanotube (SWCNT) films. Numerical simulations solving electromagnetic field and heat transfer problems revealed the MIH mechanism; the electric current induced by the applied microwave enables direct Joule heating of the SWCNT networks in the composite film. Consequently, the composite films could be heated to the target temperatures (800–1400 °C) and free-standing HC/SWCNT anodes could be prepared by applying MIH for only 30 s. Comparative analyses confirmed that ultrafast MIH is a reliable technique for producing HC anodes and can replace conventional carbonization processes which require a high-temperature furnace. Moreover, the HC/SWCNT anodes prepared by the ultrafast MIH were successfully applied to the SIB full cells. Finally, the feasibility of MIH for scalable roll-to-roll production of HC anodes was verified through local heating tests using a circular sheet larger than a resonator.

1. Introduction

With the rapid increase in the use of electric vehicles and portable mobile devices in modern society, developing inexpensive, environmentally friendly, and high-energy–density storage systems is necessary. Recently, sodium-ion batteries (SIBs) have been actively studied as promising alternatives to lithium-ion batteries (LIBs) because they are expected to compensate for the high cost of lithium sources due to scarcity [1]. Sodium sources are much cheaper, more abundant, and more environmentally friendly than lithium. Life-cycle assessments of SIBs have shown that they are promising alternatives considering the environmental impact per unit of electrical energy of battery cells [2,3]. Nevertheless, because of the low technical maturity of SIBs, high-performance active materials and cost-effective manufacturing processes with economic advantages should be developed for their commercial success [1,4].

Hard carbons (HCs) exhibit the best electrochemical performance among the various anode materials used for SIBs [5,6]. HCs are carbonaceous materials that do not graphitize even when subjected to high-temperature carbonization but develop crystal domains with an interlayer interval of approximately 0.4 nm, capable of storing sodium ions at nearly 0 V versus Na/Na+. HCs can provide more active sites on their edges, nanopores, and heteroatoms, where sodium ions are adsorbed/desorbed. Advanced HC anodes exhibit high gravimetric capacities

* Corresponding authors.
E-mail addresses: dongyunlee@knu.ac.kr (D. Yun Lee), kdh@keri.re.kr (D. Kim), jhpark79@keri.re.kr (J. Hwan Park).
[1] These authors contribute equally to this work.

https://doi.org/10.1016/j.cej.2024.154081
Received 2 May 2024; Received in revised form 11 July 2024; Accepted 16 July 2024
Available online 17 July 2024

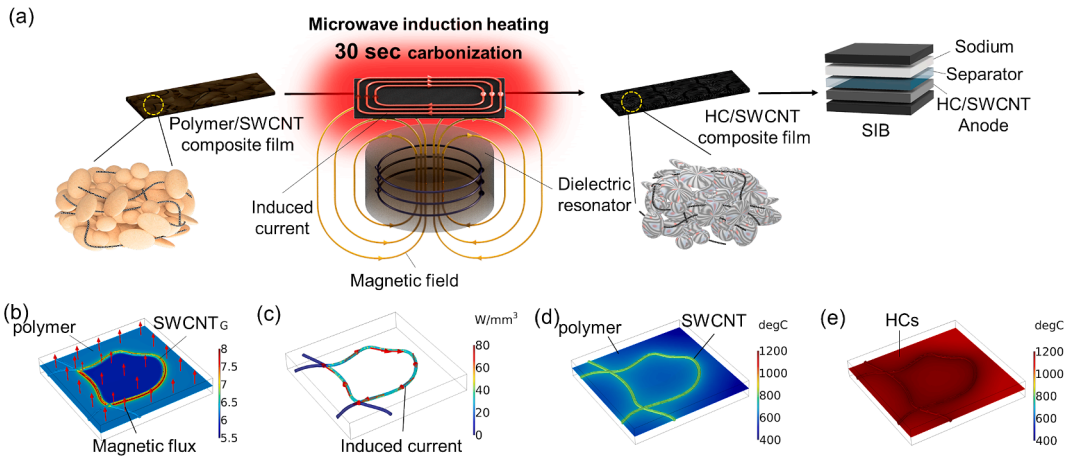

Fig. 1. (a) Schematic of the ultrafast preparation of HC anodes for SIBs via MIH of polymer/SWCNT composite films. Microscale multiphysics simulation of the MIH process reveals the (b) magnetic flux vector (length-scaled red arrows) and amplitude distribution (rainbow color), (c) induced current (length-scaled red arrows) and heating power density distribution on the SWCNT (rainbow color), (d) temperature distribution of the polymer/SWCNT before carbonization, and (e) temperature distribution of the HC/SWCNT after carbonization.

(>300 mAh/g) and excellent cycling stability.

HCs can be synthesized through the high-temperature (typically > 1000 °C) carbonization of industrial wastes [7], biomasses [8,9], and synthetic resins [10,11], which require batch-type high-temperature furnaces (HFs) under high vacuum or inert gas conditions. Long residence times (typically > several hours) at the target temperature are inevitably needed to completely carbonize the precursors because heat must be transferred from the heaters outside the chamber. Therefore, HC production in HFs requires excessive thermal energy and a considerable amount of time. In addition, shredding/grinding processes, which are energy- and time-consuming, are necessary to prepare micro-sized HC powders, followed by conventional slurry-based anode-manufacturing methods [12]. Therefore, the preparation process of HC films for SIB anodes can be simplified and made more cost-effective by replacing the heating method with contactless and direct heating technology. Induction heating using gigahertz frequencies, called microwave induction heating (MIH), can remotely heat conductive films by ohmic heat generation due to electromagnetically induced current [13]. Because MIH can directly transfer energy to materials, the required energy for carbonization and heating can be immediately supplied to accelerate the

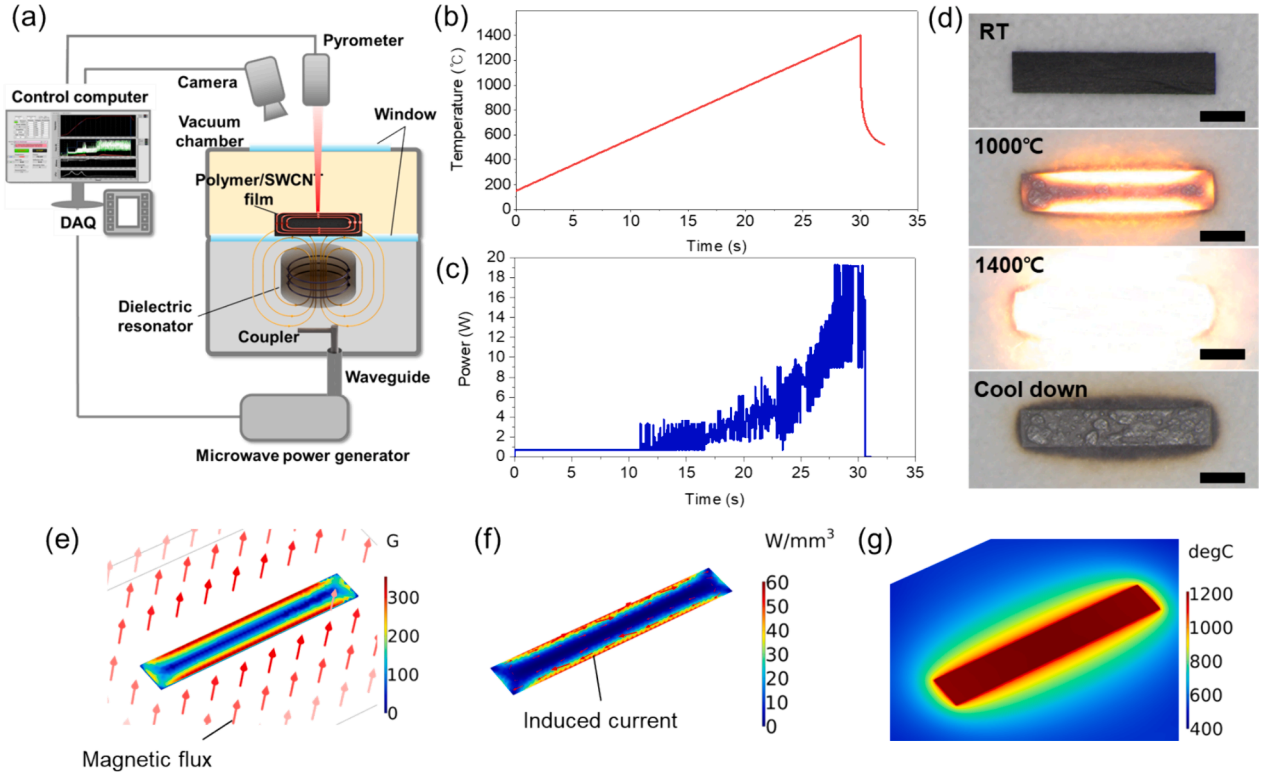

Fig. 2. (a) Schematic of the MIH system, (b) temperature profile and (c) controlled microwave power plot, and (d) camera images of the composite film during the MIH. (Scale bar = 1 mm) Macroscale multiphysics simulations reveal the (e) magnetic flux vector (length-scaled red arrow) and amplitude distribution on the film (rainbow color), (f) induced current (length-scaled red arrow) and heating power density distribution (rainbow color), and (g) temperature distribution of the film at the final heating.

thermal process with high energy efficiency.

This study successfully demonstrated an ultrafast process for producing HC anodes for SIBs through MIH of polymer/single-walled carbon nanotube (SWCNT) composite films. Electromagnetically induced current through the highly conductive SWCNT networks enabled direct Joule heating of surrounding polymer matrix or micron-sized particles. The heating mechanism of the polymer/SWCNT composite films by the MIH process was elucidated by multiscale multiphysics simulations, including electromagnetic and thermal modeling. The MIH system for film carbonization utilized a precisely controlled microwave chamber operating at 2.45 GHz, the same as a conventional microwave oven. Comparative characterization and electrochemical measurements of the prepared anodes confirmed that ultrafast MIH can reliably produce HC anodes and can replace conventional HF-based carbonization processes. Moreover, the coin-type full cell tests confirmed that the HC anodes prepared by the ultrafast MIH technique could be applied to the SIB full cells. Finally, the feasibility of MIH for large-scale HC production was demonstrated by carbonizing a circular sheet larger than a resonator.

2. Materials and methods

2.1. Preparation of polymer/SWCNT composite films

In this study, the two types of polymer precursors, carboxymethyl cellulose (CMC) and microcrystalline cellulose (MCC, 20 μm, Sigma Aldrich) powders, were used for the ultrafast MIH experiments.

The CMC/SWCNT paste (3 wt% SWCNTs) was prepared by mixing commercial CMC/SWCNT paste (TUBALL^{TM} BATT H_2O, 40 wt% of SWCNT) and sodium-CMC (Sigma Aldrich). Conductive composite films with 97 wt% of CMC and 3 wt% of SWCNTs were prepared through drop-casting of CMC/SWCNT paste, followed by room-temperature drying. (Fig. S1a) By increasing the solid content of pastes, thicker composite films can be obtained. The thickness of composite films ranged from 50 to 200 μm.

Before preparing the MCC/SWCNT composite films, the MCC powders were pre-carbonized at 400 °C for 1 h in an argon-filled Quartz tube reactor. [14] The dispersion of MCC/SWCNT was prepared by mixing MCC and SWCNT powders at a weight ratio of 90:10 in ethanol by using a horn sonicator. The MCC/SWCNT composite films were obtained by the vacuum filtration of the MCC/SWCNT dispersion. (Fig. S2a-d).

The dispersion of sodium vanadium phosphate ($Na_3V_2(PO_4)_3$, NVP, MTI Korea) and SWCNT was prepared by mixing NVP and SWCNT powders at a weight ratio of 90:10 in ethanol by using a horn sonicator. The NVP/SWCNT composite films were also obtained by the vacuum filtration of the dispersion. (Fig. S3).

2.2. Preparation of HC/SWCNT anodes

The CMC/SWCNT or MCC/SWCNT films were placed inside the metal chamber of the purpose-built MIH system comprising a dielectric resonator and a microwave coupler (2.45 GHz) [13]. The fireproof alumina sheets (Cotronics Corp., maximum temperature of 1600 °C) protected the dielectric resonator from the intense heat generated during the MIH experiments. All the heating experiments were conducted in a vacuum environment (~10 mTorr), and a LabVIEW® program controlled the power of the microwave power generator. Different samples were prepared by setting the target temperatures at the center to 800, 1000, 1200, and 1400 °C after the heating time of 30 s, denoted by MIH-CMC/SWCNT-800, MIH-CMC/SWCNT-1000, MIH-CMC/SWCNT-1200, MIH-CMC/SWCNT-1400, MIH-MCC/SWCNT-800, MIH-MCC/SWCNT-1000, MIH-MCC/SWCNT-1200, and MIH-MCC/SWCNT-1400, respectively. For comparison, the CMC/SWCNT and MCC/SWCNT films were carbonized at the temperatures of 800, 1000, 1200, and 1400 °C (HF-CMC/SWCNT-800, HF-CMC/SWCNT-1000, HF-CMC/SWCNT-1200, HF-CMC/SWCNT-1400, HF-MCC/SWCNT-800, HF-MCC/SWCNT-1000, HF-MCC/SWCNT-1200, and HF-MCC/SWCNT-1400) using graphite crucibles (Tera Leader) under an argon gas flow. The temperature of the crucible was increased to the target temperature over 1 h and then maintained for another 1 h.

2.3. Characterization and measurements

The morphology and crystal structures of the prepared samples were analyzed using SEM (Hitachi S4800), FE-TEM (FEI, Titan G2), and XRD (Panalytical, Empyrean), respectively. The BET surface area analysis and BJH pore size/volume analyses were performed using BELSORP-max equipment (MicrotracBEL, Corp.). Quantitative studies on the surface functional groups before and after carbonization were conducted using XPS (ESCALAB 250Xi analyzer). Raman analysis data was obtained using a micro-Raman spectrometer (NRS-3300, JASCO).

2.4. Multiphysics simulation

Numerical simulations of MIH were conducted using the COMSOL Multiphysics® software [15]. A complex simulation model composed of an electromagnetic field problem with a frequency domain solver and a heat transfer problem with a time domain solver was built to reveal the MIH mechanism in the composite film. The physical parameters used in the calculation are summarized in Table S1 [16–27].

2.5. Electrochemical testing

The prepared freestanding composite films were used as SIB anodes and cathodes without additional binders or conductive materials. The mass loading of the anodes, calculated from the total mass of the electrodes, was 1.0–2.0 mg cm^{-2} for the MIH-CMC/SWCNT films and 9.7–10.9 mg cm^{-1} for MIH-MCC/SWCNT films, respectively. For the NVP/SWCNT cathodes, the mass loading ranged from 20.5 to 23.0 mg cm^{-2} (2.1–2.3 mAh cm^{-2}). Coin-type half-cells (Hohsen, 2032) comprising an electrode, a glass fiber separator (GF/A, Whatman), an electrolyte, and sodium metal were assembled in an argon-filled glove box. A diethylene glycol dimethyl ether solvent (Diglyme, Sigma Aldrich) containing 1 M sodium hexafluorophosphate ($NaPF_6$, Sigma Aldrich) salt was used as the electrolyte. The coin cells' charge/discharge, electrochemical impedance spectroscopy (EIS), and cyclic voltammetry (CV) characteristics were evaluated using a potentiostat/galvanostat (VMP3, Bio-Logics).

In the half cell tests for HC/SWCNT anodes, the constant-current constant-voltage (CCCV) and constant-current (CC) modes were used for charging and discharging, respectively. A constant charge and discharge current density of 0.02 A g^{-1}_{anode} was applied for pre-cycling in the 0–2.5 V (vs. Na/Na$^+$). The cut-off current density in the CCCV mode was set to 0.002 A g^{-1}_{anode}. For long-term cycling tests, a charge/discharge current density of 0.1 A g^{-1}_{anode} and a cut-off current density of 0.01 A g^{-1}_{anode} were applied in the same voltage range. For the cycling tests at high C-rate, a charge/discharge current density of 1.0 A g^{-1}_{anode} and a cut-off current density of 0.1 A g^{-1}_{anode} were applied. The CV tests were conducted at scanning speeds of 0.2, 0.5, 1.0, 2.0, and 5.0 mV/s in the 0–2.5 V (vs. Na/Na$^+$). In the half cell tests for NVP/SWCNT cathodes, a constant charge and discharge current density of 0.01 A $g^{-1}_{cathode}$ was applied for pre-cycling in the 2.2–3.8 V (vs. Na/Na$^+$). For long-term cycling tests, a charge/discharge current density of 0.05 A $g^{-1}_{cathode}$ was applied in the same voltage range.

The coin-type full cells were assembled in an argon-filled glove box using an MIH-MCC/SWCNT anode, an NVP/SWCNT cathode, a glass fiber separator (GF/F, Whatman), and an electrolyte. In the pre-cycling, a constant charge/discharge current density of 0.01A $g^{-1}_{cathode}$ (~0.1C) was applied in the voltage range of 1.5–3.8 V (vs. Na/Na$^+$). A constant charge/discharge current density of 0.05 A $g^{-1}_{cathode}$(~0.5C) was applied in the same voltage range for the long-term cycling test.

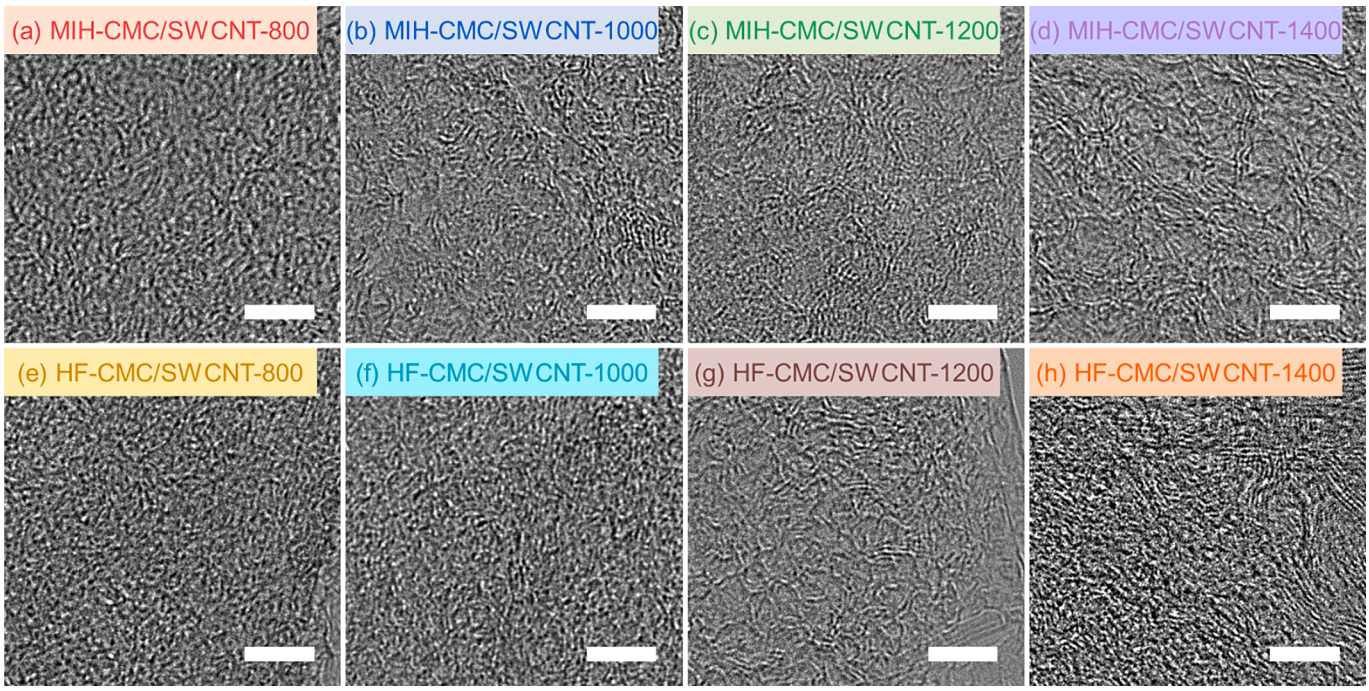

Fig. 3. FE-TEM images of (a-d) MIH-CMC/SWCNT and (e-h) HF-CMC/SWCNT films. (Scale bar = 5 nm).

3. Results and discussion

Fig. 1a schematically shows the preparation of a free-standing HC anode via ultrafast MIH. The CMC and MCC powders were used as the HC precursors. [28] The SWCNTs in the composite film created electric current networks, which act as resistive heat sources by magnetic induction in the microwave resonator. The CMC and MCC powders in the composite film are directly converted to HCs at a high temperature. Since HCs are electrically conductive, the entire film can be heated by the induced currents. Therefore, rapid carbonization from polymer precursors to HCs could be achieved in 30 s with the remote and direct heat energy generated by MIH. The prepared HC/SWCNT films were used as SIB anodes without post-carbonization procedures because the SWCNTs also served as conductive auxiliaries and binders. This innovative technique effectively reduces the carbonization time and complexity of the anode manufacturing processes.

In this study, a novel heating method by magnetic induction using a dielectric resonator was developed [13]. MIH differs from the dielectric heating mechanism in conventional microwave ovens which rely on a metal cavity resonator. The resonant magnetic field in the dielectric resonator rotates from the center of the resonator to the outside, forming a toroidal electric field similar to that of a solenoid coil, which selectively applies the magnetic field to the film [29]. The magnetic field oscillating at 2.45 GHz can strongly interact with conducting and nanoscale-thin SWCNTs through magnetic induction.

The MIH mechanism for the ultrafast carbonization process was revealed via numerical multiphysics simulations, as shown in Fig. 1b–e [15]. The SWCNTs have local contacts to extend the induction current path (Fig. S1), and it is assumed that the polymers fill the rest of the space without vacancies, as shown in Fig. 1b. When a GHz magnetic field (red arrows scaled with its length shown in Fig. 1b) is applied to the SWCNT conducting loop, electric currents are induced on the conductive SWCNTs, and a self-magnetic field re-induced by the current sets off a net magnetic field inside the current loop (amplitude distribution of magnetic flux in rainbow color scale in Fig. 1b). Intense current and heat (red arrows and rainbow color plot in Fig. 1c) occur in closed loop of SWCNTs. The temperature distribution at the initial stage shows that SWCNTs have a much higher temperature than the polymers despite heat transfer (Fig. 1d). However, the insulating polymers near the SWCNTs are converted to conducting HCs over 650 °C, and the composite film is entirely heated since the HCs can now serve as active sites for MIH. Finally, the temperature gradient from the SWCNTs to the surrounding volume disappears, and uniform heating can be achieved (Fig. 1e).

Fig. 2a shows the MIH system developed in this study. The dielectric resonator is inside a metallic shield which prevents microwave radiation leakage. A solid-state microwave generator and a coaxial waveguide supply the microwave power. The microwave energy stored in the dielectric resonator is coupled via a bar coupler, which adjusts the distance to the dielectric resonator to optimize the microwave coupling between the waveguide and the resonator. The polymer/SWCNT film is positioned on top of the dielectric resonator and the two compartments are separated by a microwave-transparent quartz window to maintain a vacuum environment. The temperature of the film is measured with a pyrometer through another quartz window on top of the vacuum chamber. The heating time profile can precisely follow the programmed preset profile since the microwave power level is automatically and quickly controlled based on the measured temperature, as shown in Fig. 2b-c.

The carbonization process temperature is linearly increased to a maximum of 1400 °C in 30 s to avoid film swelling due to sudden large outgassing. Fig. 2d shows camera images of a long rectangular polymer/SWCNT composite film undergoing carbonization in the MIH chamber. The macro-flow of the induction current on the whole film is rotated by the magnetic field normal to the surface, as the numerical simulations show in Fig. 2e-f. Because the conductive film pushes out the applied magnetic field due to offset by the current-induced self-magnetic field, the current density and heating power density at the edges are stronger than those at the center of the film. Therefore, the carbonization of the film starts from the edges and expands to the center; as a result, uniform heating and carbonization can be achieved as the maximum temperature is reached after 30 s. The effect of temperature on the film is shown in Fig. 2d, and the numerical simulation result is shown in Fig. 2g. As shown in Fig. S1b-c, HC/SWCNT maintained the film morphology while micropores developed during MIH.

Field-emission transmission electron microscopy (FE-TEM) was

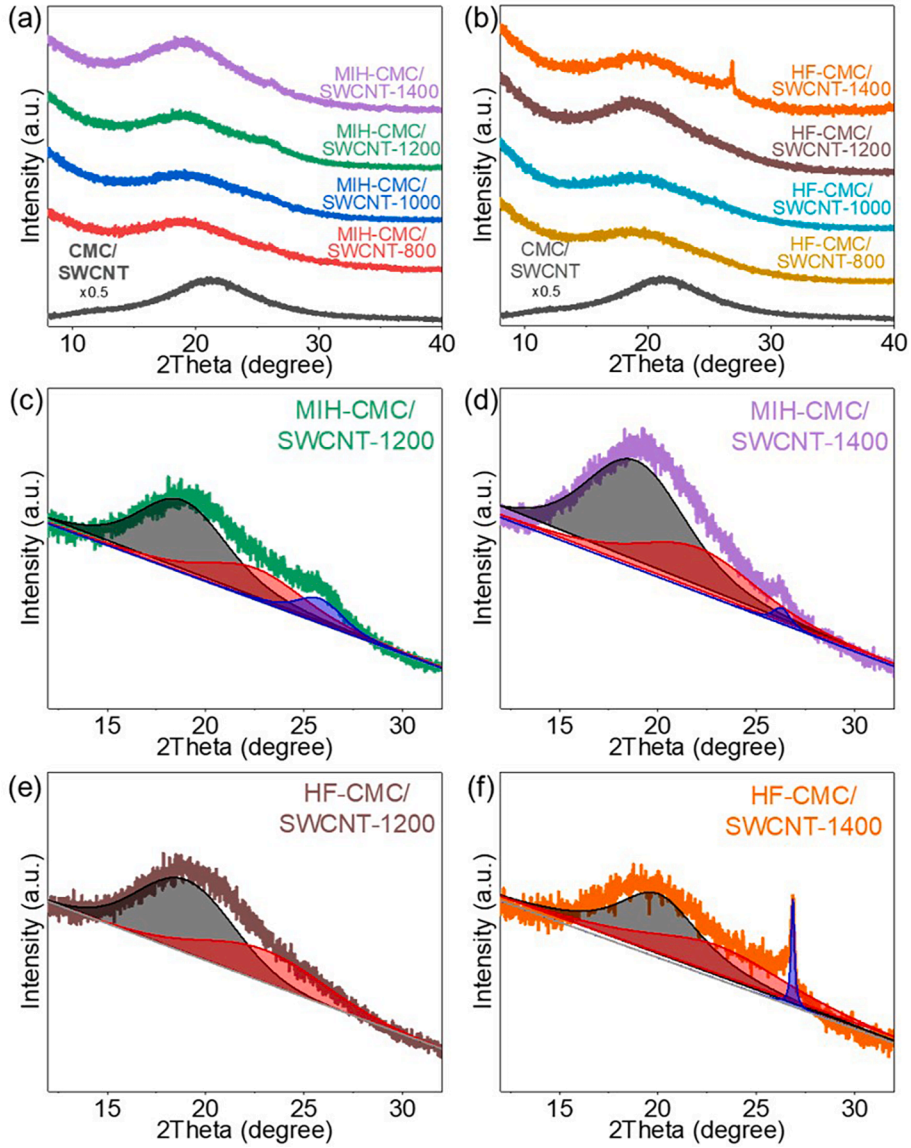

Fig. 4. XRD characterization of MIH and HF samples. (a,b) XRD patterns and (c-f) deconvolution of the (0 0 2) peaks.

conducted to characterize the microcrystalline structures of the CMC/SWCNT films carbonized with MIH and HF (Fig. 3). MIH-CMC/SWCNT-800 and HF-CMC/SWCNT-800 films exhibited highly disordered carbon structures. MIH-CMC/SWCNT-1000, MIH-CMC/SWCNT-1200, HF-CMC/SWCNT-1000, and HF-CMC/SWCNT-1200 films exhibited winding lamellar structures with short-range ordering (<5 nm). Long-range (>10 nm) lamellar structures with several carbon layers were well-developed in MIH-CMC/SWCNT-1400 and HF-CMC/SWCNT-1400 films. In particular, HF-CMC/SWCNT-1400 film exhibited highly ordered graphite-like lamellar structures. The X-ray diffraction (XRD) results support the TEM imaging results of the MIH and HF samples (Fig. 4). The CMC/SWCNT film exhibited a broad XRD peak centered at 21.6°, corresponding to the crystal structure of CMC [30]. However, MIH-CMC/SWCNT-800 and HF-CMC/SWCNT-800 films showed dramatically reduced XRD signals for CMCs, indicating disorganization of the CMC crystal domains during the carbonization up to a temperature of 800 °C (Fig. 4a-b). After that, the broad XRD signals in the range of 20–27° correspond to the highly disordered (21 ~ 22°), pseudo-graphitic (22 ~ 25°), and graphite-like (26 ~ 27°) HCs, revealing that HCs gradually developed with the increase in the carbonization temperature [31]. The deconvolution of the XRD patterns of the MIH films indicated the simultaneous development of highly disordered (black area), pseudo-graphitic (red area), and graphite-like (blue area) HC domains (Fig. 4c-d, Table S2) [32]. In contrast, HF-CMC/SWCNT-1200 film exhibited only two characteristic peaks corresponding to the highly disordered and pseudo-graphitic HC (Fig. 4e). However, HF-CMC/SWCNT-1400 film clearly showed a sharp peak emerging from broadened XRD signals at 26.9°, indicating the evolution of graphite-like HC crystal domains during HF-based carbonization (Fig. 4f). The TEM and XRD results verify that the formation of graphite-like HC is suppressed during ultrafast MIH compared to the HF-based carbonization process. The Raman spectrum of CMC/SWCNT shows SWCNTs' distinct G and G'-bands. (Fig. S4) The MIH-CMC/SWCNT-800 exhibited slightly increased signals corresponding to the disordered carbons (D-band, 1344 nm). [33] However, the increase in D-band is not direct evidence of the formation of hard carbons. During the MIH process at high temperatures, defective carbon can be formed in the SWCNTs.

Fig. 5a-d shows the prepared samples' Brunauer–Emmett–Teller (BET) isotherm and Barrett–Joyner–Halenda (BJH) pore size distribution. The bare CMC/SWCNT was a dense film with a low specific surface area of 7 m^2/g. MIH-CMC/SWCNT-800 and HF-CMC/SWCNT-800 samples exhibited significantly increased specific surface areas (SSAs)

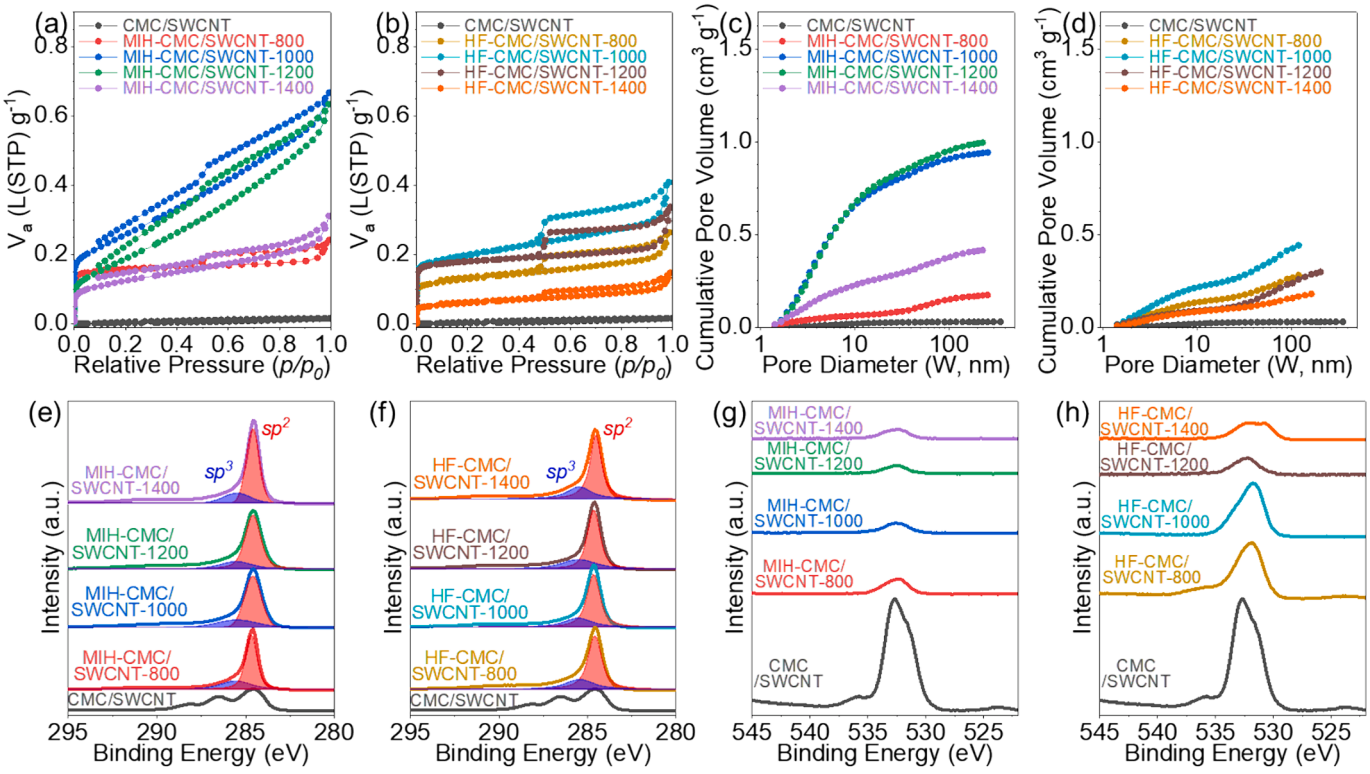

Fig. 5. (a,b) BET isotherm, (c,d) BJH pore size/volume distribution, (e,f) XPS C1s, and (g,h) XPS O1s data of MIH and HF samples.

of 612 and 467 m^2/g, respectively (Fig. S5a). The pore size distribution data indicate the formation of micro-, meso-, and macropores in the MIH-CMC/SWCNT-800 and HF-CMC/SWCNT-800 films [34]. MIH-CMC/SWCNT-1000 film showed the highest SSA of 911 m^2/g because of the significant formation of mesopores (d = 2–50 nm). Therefore, it is plausible that the formation of short-range-order lamellar structures observed in the TEM images (Fig. 3b) could have induced numerous mesopores. MIH-CMC/SWCNT-1200 film also exhibited a high SSA of 723 m^2/g and mesopore-dominated pore size distribution. However, compared with MIH-CMC/SWCNT-1200 film, the total pore volume of MIH-CMC/SWCNT-1400 film decreased from 0.99 to 0.42 $cm^3\ g^{-1}$ because of the decrease in the volume of the mesopores originating from the growth of graphitic HCs (Fig. 5c) [32]. Although HF-CMC/SWCNT-1000 film also showed increased SSA (718 m^2/g) and mesopore volume, the total pore volume was only 0.45 $cm^3\ g^{-1}$ (Fig. 5d). Moreover, HF-CMC/SWCNT-1200 and HF-CMC/SWCNT-1400 films exhibited small mesopore volumes (<0.1 $cm^3\ g^{-1}$) because of the formation of graphitic HCs. The X-ray photoelectron spectroscopy (XPS) surface analysis results suggest that the formation of sp^2 carbons and the removal of oxygen-functional groups mainly occurred during the MIH below a temperature of 800 °C (Fig. 5e-h and Fig. S5b-c). The sp^2/sp^3 carbon ratio was estimated to be 2.4 for HF-CMC/SWCNT-800, which gradually increased to 3.7 after MIH up to 1400 °C [35]. This result indicates that sp^2 carbons were well developed during carbonization by MIH. However, the carbon ratio of HF samples was not dependent on the target temperature. The oxygen contents in CMC/SWCNT, MIH-CMC/SWCNT-800, and MIH-CMC/SWCNT-1400 films were 26.5 %, 3.59 %, and 2.05 %, respectively. However, the HF samples showed a relatively high oxygen content, as estimated from the XPS data. These XPS results imply that MIH is more efficient at removing oxygen-containing functional groups because intense heat can be directly transferred from the SWCNTs to the neighboring CMCs.

Half-cells were assembled using sodium metal reference electrodes to conduct electrochemical tests on the prepared SIB anodes (Fig. 6). The CMC/SWCNT anode exhibited a low sodium-ion storage performance (Fig. S6). Fig. 6a-b shows the charge/discharge capacities of the anodes under pre-cycling normalized by the electrode weight. The initial charge/discharge capacities of MIH-CMC/SWCNT-800, MIH-CMC/SWCNT-1000, MIH-CMC/SWCNT-1200, and MIH-CMC/SWCNT-1400 anodes were 620/210, 480/252, 463/265, and 484/187 mAh g_{anode}^{-1}, respectively. The charging capacity decreased with the increase in the target MIH temperature, whereas the MIH-CMC/SWCNT-1200 anode exhibited the highest discharge capacity of 265 mAh g_{anode}^{-1}. As a result, it showed the best initial Coulombic efficiency (ICE) of 57.2 %. Among the HF anodes, the HF-CMC/SWCNT-1000 anode demonstrated the best electrochemical performance, exhibiting an initial discharge capacity of 256 mAh g_{anode}^{-1} HF-CMC/SWCNT-1200 anode showed an initial discharge capacity of 196 mAh g_{anode}^{-1}, which was inferior to that of HF-CMC/SWCNT-1000 anode. HF-CMC/SWCNT-1400 anode delivered the lowest initial discharge capacity of 106 mAh g_{anode}^{-1} with an initial Coulombic efficiency of 27.0 %. The results of the rate capability tests suggest that the MIH1200 anode showed the best performance, even at high C-rates (Fig. 6c). MIH-CMC/SWCNT-1200 anode delivered 70 mAh g_{anode}^{-1} even at 10 A/g (40C, 1.0 C=0.25 A/g) and had excellent capacity recovery characteristics at a current density of 0.02 A g_{anode}^{-1} (0.08C). As shown in Fig. 6e, MIH-CMC/SWCNT-1200 exhibits the highest initial discharge capacity of approximately 200 mAh g_{anode}^{-1} at a charge/discharge current density of 0.1 A/g (0.4 C). The discharge capacity of the MIH-CMC/SWCNT-1200 anode gradually increased to approximately 230 mAh g_{anode}^{-1} during the first 150 cycles, and the discharge capacity did not decrease until the 200th cycle. This trend can be attributed to the gradual wetting or penetration of electrolytes into the highly porous structures. [36,37] As shown in Fig. S7, the gradual filling of pores with electrolytes improves the charge storage capacity by providing additional sites for capacitive-type ion storage at high voltage regions (>1.0 V). In addition, the MIH-CMC/SWCNT-1200 anode exhibited the highest CE of 99.5 % after 200 cycles. Although all the other MIH anodes exhibited lower discharge capacities than that of MIH-CMC/SWCNT-1200, their capacity retentions were approximately 100 %. The results of the long-term stability test at a high current density

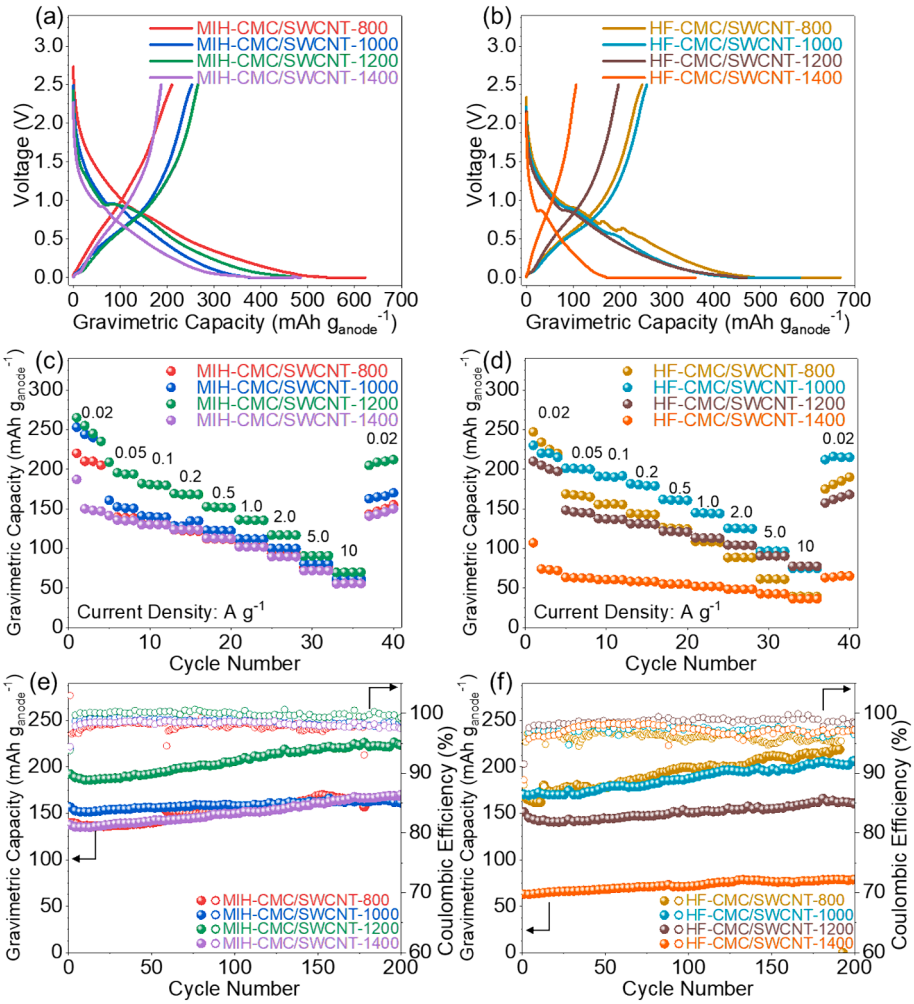

Fig. 6. (a,b) Initial sodiation–desodiation profiles, (c,d) rate capabilities, and (e,f) capacity retentions of MIH and HF anodes.

(1.0 A/g, 4C condition) also support that the MIH-CMC/SWCNT-1200 exhibited the best sodium ion storage performance (Fig. S8). As shown in Fig. S9, the cycled electrodes have well-maintained layered CMC/SWCNT structures. In addition, the cycled sodium metal anodes exhibited white surfaces, implying that the corrosion of sodium metal is not critical. In the EIS analyses, the cycled MIH-CMC/SWCNT-1200 anode exhibited the lowest charge transfer resistance (Fig. S10). The inferior rate-capability of MIH-CMC/SWCNT-1400 can be attributed to the highest series resistance. Electrochemical testing on the HF anodes showed that the HF-CMC/SWCNT-1000 anode has the best C-rate performance and the highest long-term cyclability (Fig. 6d and f). Table S3 compares the sodium-ion storage characteristics of the MIH anodes with those of other cellulose-based HC anodes [28,38–43]. Since the MIH-CMC/SWCNT-1200 anode does not require additional conductive materials or polymeric binders, it showed a commensurate performance compared with conventional HC anodes, demanding 10–20 wt% of binders and conductive auxiliaries.

Based on these results, we conclude that ultrafast MIH is a reliable technique for producing HC anodes as an alternative to the conventional HF-based carbonization method. The pore/crystal structures determining the electrochemical performance could be readily controlled by adjusting the target temperature of the ultrafast MIH. The anode performance of the best MIH anode was not inferior to that of the best HF anode, although the optimum final temperature of MIH increased from 1000 to 1200 °C.

To determine the cause of the shift in the optimum carbonization temperature, CV analyses were conducted for MIH and HF anodes (Fig. 7 and Fig. S11). The $v/v^{1/2}$ scan rate analyses on the anodes make it possible to quantitatively estimate the relative contribution and the absolute amount of diffusive and capacitive stored charge [44–46].

The total CV signals at a given voltage (V) can be expressed by the sum of the capacitive and diffusion-controlled currents.

$$i(V) = k_1(V)v + k_2(V)v^{1/2} \quad (1)$$

where k_1 and k_2 are the scan rate constants. By plotting $i/v^{1/2}$ against $v^{1/2}$ at a given potential, the scan rate constant can be estimated using the following equation:

$$i(V)/v^{1/2} = k_1(V)v^{1/2} + k_2(V) \quad (2)$$

Accordingly, the contributions of the capacitive (k_1v) and diffusion-controlled ($k_2v^{1/2}$) charge storage can be evaluated. The rate dependency of the CV curves was studied at various scan rates. (Fig. S11). The $v/v^{1/2}$ scan rate analysis results of the MIH anodes reveal that MIH-CMC/SWCNT-1200 exhibits the highest total stored charge (1565C/g) and contributes the least to capacitive sodium ion storage (45 %) at a scan rate of 0.2 mV/s (Fig. 7c and i). Although MIH800 anode exhibited the lowest total stored charge of 1010C/g, it showed the most considerable stored charge and contribution from the capacitive mechanism (755C/g, 75 %, Fig. 7a). The diffusively stored charges of MIH-CMC/SWCNT-1000 (565 C/g) and MIH-CMC/SWCNT-1200 anodes (855 C/g) were more significant than those of MIH-CMC/SWCNT-800 anode (255 C/g). This is attributed to the large mesopore volume of the two anodes (Fig. 5c), which benefits Na-ion intercalation/deintercalation

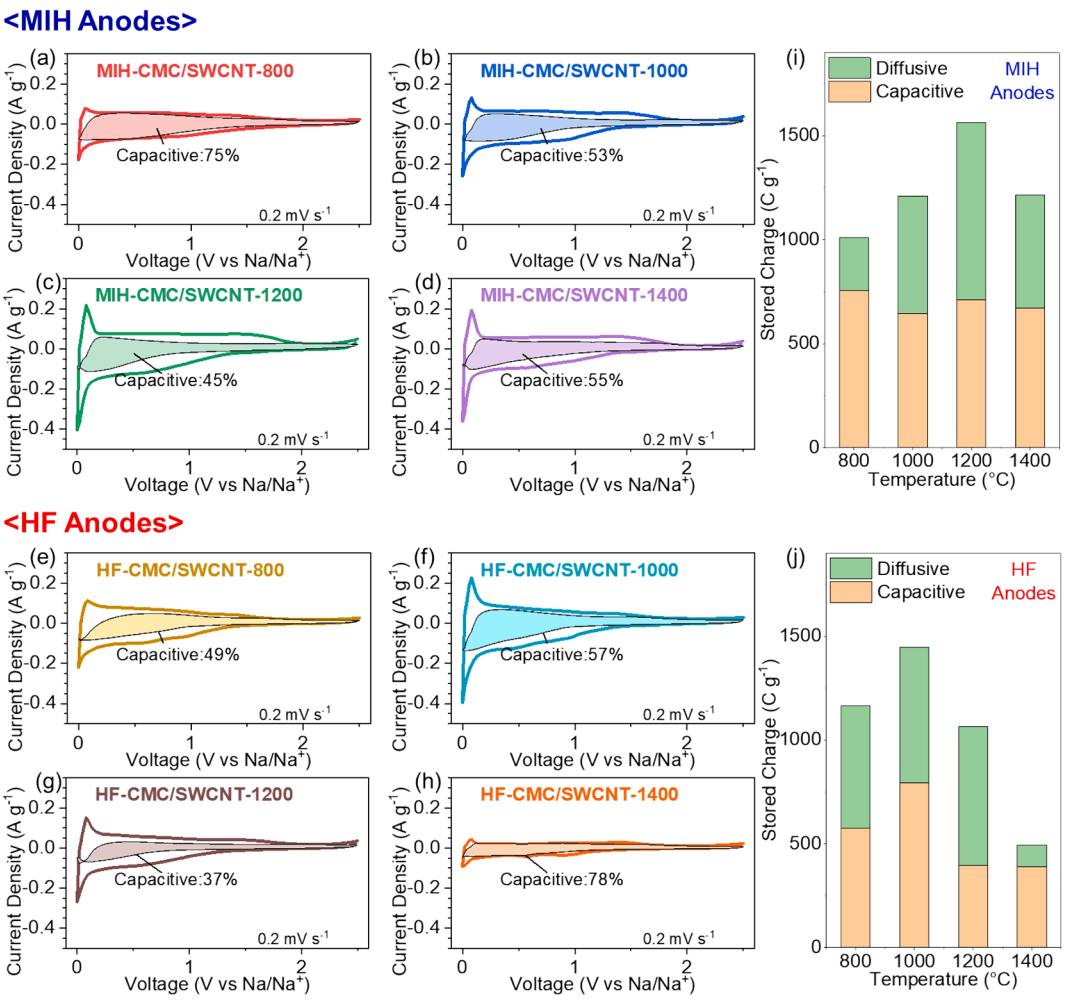

Fig. 7. Deconvolution of CV curves: CV curves of (a-d) MIH and (e-h) HF anodes with capacitive currents ($k_1\upsilon$, filled area). Bar graphs of the stored charge via capacitive and diffusive mechanisms for (i) MIH and (j) HF anodes.

[47,48]. Moreover, pseudo-graphitic lamellar structures that can store sodium ions were well-developed in the MIH-CMC/SWCNT-1200 anode. In contrast, the MIH-CMC/SWCNT-1400 anode exhibited a lower total storage charge (1215C/g) than the MIH-CMC/SWCNT-1200 anode, and a declined stored charge via a diffusive mechanism (855 → 545 C/g). The developed graphitic HC domains clogged the mesopores (Fig. 5c), and sodium ions could hardly be stored in the lamellar structures of the HCs. Among the HF anodes, the HF-CMC/SWCNT-1000 anode showed the highest capacitive (795 C/g) and total stored charge (1445C/g) at a scan rate of 0.2 mV/s (Fig. 7j). HF-CMC/SWCNT-1200 anode exhibited a much-reduced capacitive storage capacity because its clogged pores limited surface adsorption (Fig. 5d). In particular, the diffusively stored charge of HF-CMC/SWCNT-1400 anode was 105 C/g, resulting in the lowest total stored charge (495 C/g) because the graphitic HC domains unsuitable for sodium ion intercalation dramatically developed during HF-based annealing at 1400 °C. Consequently, the sodium ion storage capacity of the HF-CMC/SWCNT-1400 anode primarily depends on the contribution of the capacitive mechanism (78 %). Compared to the MIH, HF-based carbonization suppressed pore development but facilitated the formation of crystalline HCs, resulting in a lower shift in the optimum carbonization temperature. From the CV test results in Fig. S11, the sodium-ion diffusion coefficient (D_{Na}^{+}) of MIH anodes can be estimated according to the classical Randles-Sevcik equation.[49] The peak current (I_p) of reduction or oxidation can be estimated by the following equation:

$$I_p = (2.69 \times 10^5) n^{1.5} A D_{Na^+}^{0.5} \nu^{0.5} C_{Na^+} \quad (3)$$

where n is the number of electrons transferred, A is the electrode area, C_{Na}^{+} is the sodium-ion concentration in the electrolyte, and υ is the scanning rate (V s^{-1}). Fig. S12 shows the linear relationship of the reduction and oxidation peak current density with the square root of voltage scanning rates for sodium ion intercalation region (~0 V vs. Na/Na^+). As a result, the MIH-CMC/SWCNT-1200 anode displays the highest D_{Na}^{+} (49.1 × 10^{-6} cm^2 s^{-1}), supporting the largest diffusive capacity of MIH-CMC/SWCNT-1200 (Fig. 7i).

We conducted MIH of MCC/SWCNT composite films to prove another concept. (Fig. 8a). The MCC microparticles (Fig. S2a) were used to prepare MCC/SWCNT bucky papers (Fig. S2b-d). Before preparing bucky papers, the MCC powders were pre-carbonized at 400 °C to increase the wt.% of HCs in final HC/SWCNT anodes.[14] Electromagnetically induced current through the highly conductive SWCNT networks enabled direct Joule heating of surrounding MCC microparticles. The MCC/SWCNT anode exhibited poor initial charge/discharge capacities of 169/109 mAh g_{anode}^{-1}. Fig. S13 shows the pre-cycling test results of HF-MCC/SWCNT anodes. Among the HF-MCC/SWCNT anodes, the HF-MCC/SWCNT-1200 displayed the best initial charge/discharge capacities and ICEs of 298/379 (78.6 %). On the other hand, by applying MIH, the MCC/SWCNT bucky papers were rapidly heated to 800–1400 °C in the 30 s, resulting in MIH-MCC/SWCNT anodes (Fig. S2e-f). Fig. 8b shows the anode's initial charge/discharge capacities normalized by the electrode weight. The initial charge/discharge

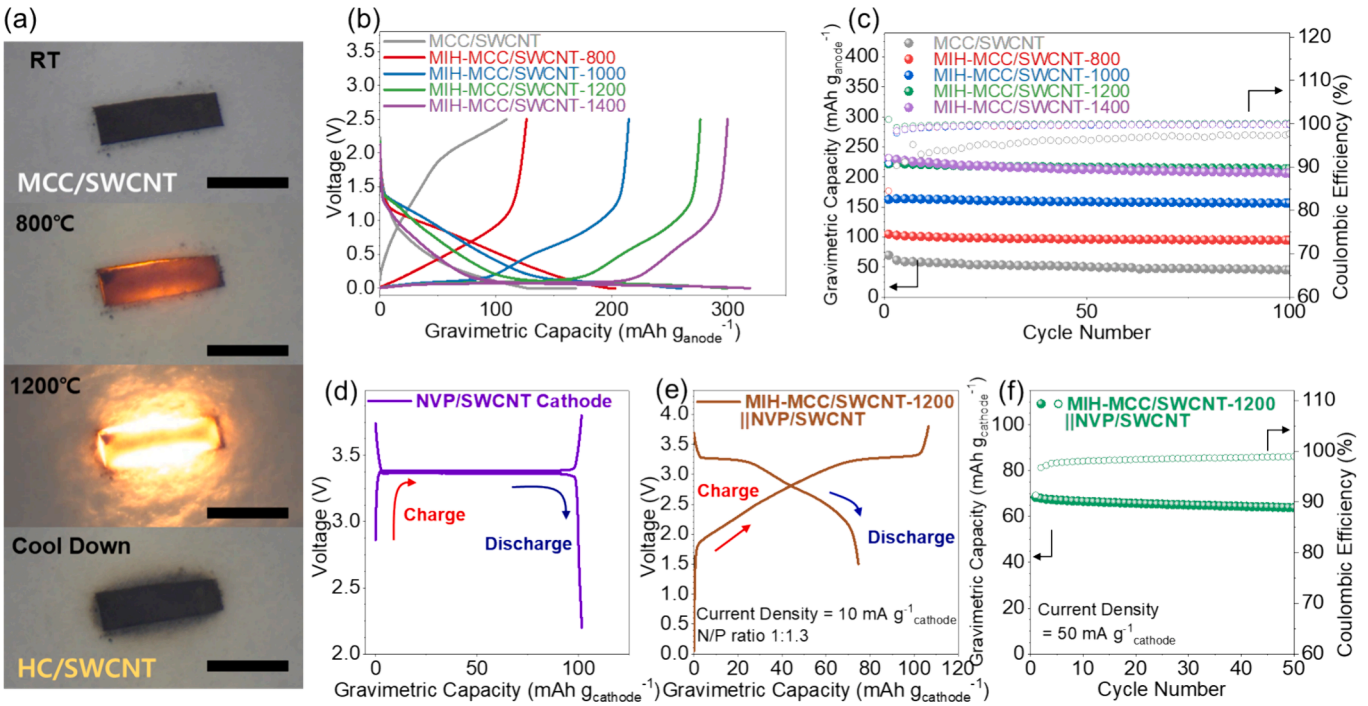

Fig. 8. (a) The camera images of the MCC/SWCNT and MIH-MCC/SWCNT composite films during the MIH. (Scale bar = 5 mm) (b) Initial sodiation–desodiation profiles, and (c) capacity retentions of MCC/SWCNT, MIH-MCC/SWCNT-800, MIH-MCC/SWCNT-1000, MIH-MCC/SWCNT-1200, and MIH-MCC/SWCNT-1400 half cells. (d) Initial charge–discharge profiles of NVP/SWCNT half cell. (e) Initial charge–discharge profiles and (f) capacity retentions of MIH-MCC/SWCNT-1200||NVP/SWCNT full cell.

capacities and ICEs of MIH-MCC/SWCNT-800, MIH-MCC/SWCNT-1000, MIH-MCC/SWCNT-1200, and MIH-MCC/SWCNT-1400 anodes were 203/126 (62.1 %), 260/215 (82.7 %), 299/276 (92.3 %), and 319/300 (94.0 %) mAh g^{-1}_{anode}, respectively. Among the MIH-MCC/SWCNT anodes, the MIH-MCC/SWCNT-1200 exhibited the highest capacity retention of 96.5 % after 100 cycles (221.8 → 214.0 mAh g^{-1}_{anode}). Although the MIH-MCC/SWCNT-1400 exhibited a slightly higher discharge capacity of 230.7 mAh g^{-1}_{anode} at the first cycle, it showed a lower capacity retention of 89.6 % after 100 cycles. The MIH-MCC/SWCNT-800 and MIH-MCC/SWCNT-1000 displayed inferior discharge capacities of 162.4 and 104.9 mAh g^{-1}_{anode} at the first cycle. Therefore, these results also support the idea that the MIH technique is suitable for the ultrafast heating of polymeric microparticle/SWCNT composite films.

The SIB full cells were prepared by assembling the MIH-MCC/SWCNT-1200 anodes and the NVP/SWCNT cathodes. The N/P ratio of the full cell was calculated based on the initial discharge capacities of the MIH-MCC/SWCNT-1200 anodes and the NVP/SWCNT cathodes. As shown in Fig. 8d, the initial discharge capacity of the NVP/SWCNT cathode was determined to be 101.7 mAh $g^{-1}_{cathode}$ In addition, the superior capacity retention of the cathode was confirmed in the long-term cycling tests (97.0 % @ 100th cycle, Fig. S14). We paired anodes and cathodes to achieve an N/P ratio of 1.2–1.3. [50] As summarized in Fig. 8e-f and Table S4, the ICE (71.6 %), initial discharge capacity (74.7 mAh $g^{-1}_{cathode}$), and capacity retention (93.3 % @ 50th cycles) of the MIH-MCC/SWCNT-1200||NVP/SWCNT full cell were comparable to those of the recently reported HC||NVP full cells.[50–54] Therefore, the results support that the HC anodes prepared by the ultrafast MIH technique can be applied to the SIB full cells.

To determine the feasibility of MIH for the scalable production of HC anodes, the process was evaluated using a large circular polymer/SWCNT sheet (d = 4.2 cm). Fig. 9a shows a conceptual schematic of MIH. The circular sheet, larger than the resonator and heated to 1200 °C in 30 s, shows a circular-ring-shaped uniform heating zone (Fig. 9b). Thus, an MIH system with a dielectric resonator array is feasible for roll-to-roll manufacturing of uniform HC/SWCNT anodes (Fig. 9c). The polymer/SWCNT film moves above the dielectric resonator array, resulting in HC/SWCNT anodes. Simultaneously, each heating zone is maintained at the target temperature by precisely adjusting the power level of the microwave generator.

4. Conclusions

We performed MIH-assisted carbonization of polymer/SWCNT films to realize an ultrafast production of HC anodes for SIBs. This strategy significantly reduces the carbonization time owing to direct heating from the inside of the composite films and eliminates the need for slurry-based electrode manufacturing processes after carbonization. Free-standing and binder-free HC/SWCNT anodes could be prepared from CMC/SWCNT and MCC/SWCNT films with precisely controlled target temperatures of 800–1400 °C in only 30 s through a novel MIH device based on a specially designed dielectric resonator. The results of physicochemical and electrochemical characterization indicate that MIH is a reliable technique for producing HC anodes and is an excellent alternative to the conventional HF-based carbonization method. The full cell tests confirmed that the HC anodes prepared by the ultrafast MIH technique could be applied to the SIB full cells. Moreover, MIH's application to a large circular sheet was demonstrated, revealing the scalability of MIH. Overall, the MIH of the composite films is expected to aid in the mass production of HC anodes, which is crucial for commercializing SIBs.

CRediT authorship contribution statement

Gyeongbeom Ryoo: Writing – review & editing, Writing – original draft, Validation, Methodology, Investigation, Data curation, Conceptualization. **Jiwon Shin:** Writing – review & editing, Writing – original draft, Validation, Methodology, Investigation, Data curation, Conceptualization. **Byeong Guk Kim:** Resources, Data curation. **Do Geun Lee:** Resources, Data curation. **Joong Tark Han:** Resources, Funding

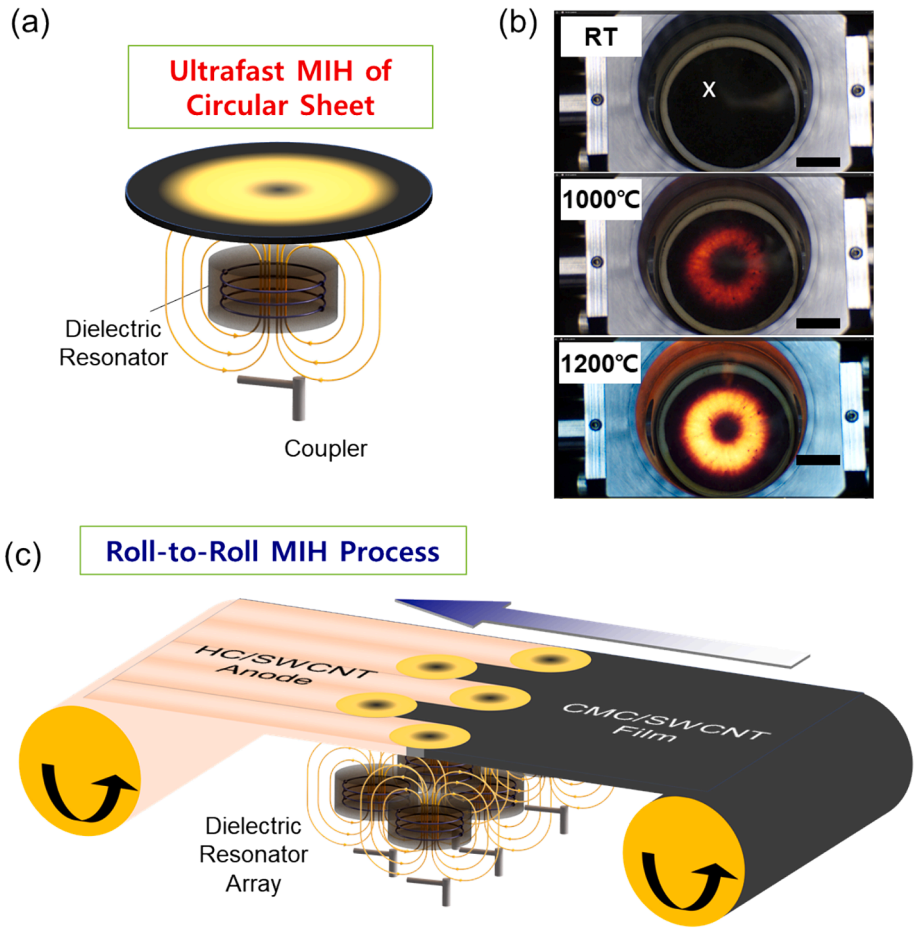

Fig. 9. (a) Schematic and (b) camera images of MIH carbonization of a circular sheet. The microwave power is automatically controlled so that the measured temperature at point "X" follows the programmed preset profiles (Scale bar = 1 cm). (c) Conceptual schematic of roll-to-roll MIH process for scalable HC/SWCNT anodes production.

acquisition. **Byeongho Park:** Resources, Data curation. **Youngseok Oh:** Resources, Funding acquisition. **Seung Yol Jeong:** Investigation. **Se-Hee Lee:** Resources. **Dong Yun Lee:** Validation, Supervision, Resources, Investigation. **Daeho Kim:** Writing – review & editing, Supervision, Methodology, Funding acquisition, Conceptualization. **Jong Hwan Park:** Writing – review & editing, Writing – original draft, Validation, Supervision, Methodology, Conceptualization.

Declaration of competing interest

The authors declare that they have no known competing financial interests or personal relationships that could have appeared to influence the work reported in this paper.

Data availability

Data will be made available on request.

Acknowledgments

G. Ryoo and J. Shin contributed equally to this work. This research was supported by the Primary Research Program (24A01022) of Korea Electrotechnology Research Institute, the National Research Council of Science & Technology (NST) grant by the Korea government (MSIT) (No. CAP21041-100), and the Research Fund of the Korea Institute of Materials Science (No. PNKA100).

Appendix A. Supplementary data

Supplementary data to this article can be found online at https://doi.org/10.1016/j.cej.2024.154081.

References

[1] C. Vaalma, D. Buchholz, M. Weil, S. Passerini, A cost and resource analysis of sodium-ion batteries, Nat. Rev. Mater. 3 (2018) 18013, https://doi.org/10.1038/natrevmats.2018.13.
[2] J. Peters, D. Buchholz, S. Passerini, M. Weil, Life cycle assessment of sodium-ion batteries, Energy Environ. Sci. 9 (2016) 1744, https://doi.org/10.1039/C6EE00640J.
[3] J.F. Peters, M. Baumann, J.R. Binder, M. Weil, On the environmental competitiveness of sodiumion batteries under a full life cycle perspective – a cell-chemistry specific modelling approach, Sustainable Energy Fuels 5 (2021) 6414, https://doi.org/10.1039/D1SE01292D.
[4] K.M. Abraham, How comparable are sodium-ion batteries to lithium-ion counterparts? ACS Energy Lett. 5 (2020) 3544–3547, https://doi.org/10.1021/acsenergylett.0c02181.
[5] J. Ding, W. Hu, E. Paek, D. Mitlin, Review of hybrid ion capacitors: From aqueous to lithium to sodium, Chem. Rev. 118 (2018) 6457–6498, https://doi.org/10.1021/acs.chemrev.8b00116.
[6] X. Dou, I. Hasa, D. Saurel, C. Vaalma, L. Wu, D. Buchholz, D. Bresser, S. Komaba, S. Passerini, Hard carbons for sodium-ion batteries: Structure, analysis, sustainability, and electrochemistry, Mater. Today 23 (2019) 87–104, https://doi.org/10.1016/j.mattod.2018.12.040.
[7] Y. Li, M.P. Paranthaman, K. Akato, A.K. Naskar, A.M. Levine, R.J. Lee, S.-O. Kim, J. Zhang, S. Dai, A. Manthiram, Tire-derived carbon composite anodes for sodium-ion batteries, J. Power Sources 316 (2016) 232–238, https://doi.org/10.1016/j.jpowsour.2016.03.071.
[8] M. Thompson, Q. Xia, Z. Hu, X.S. Zhao, A review on biomass-derived hard carbon materials for sodium-ion batteries, Mater. Adv. 2 (2021) 5881, https://doi.org/10.1039/D1MA00315A.

[9] D. Alvira, D. Antorán, J.J. Manyà, Plant-derived hard carbon as anode for sodium-ion batteries: A comprehensive review to guide interdisciplinary research, Chem. Eng. J. 447 (2022) 137468, https://doi.org/10.1016/j.cej.2022.137468.

[10] H.-L. Wang, Z.-Q. Shi, J. Jin, C.-B. Chong, C.-Y. Wang, Properties and sodium insertion behavior of phenolic resin-based hard carbon microspheres obtained by a hydrothermal method, J. Electroanal. Chem. 755 (2015) 87–91, https://doi.org/10.1016/j.jelechem.2015.07.032.

[11] A. Beda, P.-L. Taberna, P. Simon, C.M. Ghimbeu, Hard carbons derived from green phenolic resins for Na-ion batteries, Carbon 139 (2018) 248–257, https://doi.org/10.1016/j.carbon.2018.06.036.

[12] J.F. Peters, M. Abdelbaky, M. Baumann, M. Weil, A review of hard carbon anode materials for sodium-ion batteries and their environmental assessment, Matériaux Techniques 107 (2019) 503, https://doi.org/10.1051/mattech/2019029.

[13] D. Kim; Korea Electrotechnology Research Institute. Microwave band induction heating device. US20220279629. 2022 Sep 1.

[14] Y. Zhen, Y. Chen, F. Li, Z. Guo, Z. Hong, M.-M. Titirici, Ultrafast synthesis of hard carbon anodes for sodium-ion batteries, Proc. Natl. Acad. Sci. 118 (2021), https://doi.org/10.1073/pnas.2111119118 e2111119118.

[15] COMSOL Multiphysics®, COMSOL AB, Stockholm, Sweden.

[16] K. Daicho, K. Kobayashi, S. Fujisawa, T. Saito, Crystallinity-independent yet modification-dependent true density of nanocellulose, Biomacromolecules 21 (2020) 939–945, https://doi.org/10.1021/acs.biomac.9b01584.

[17] X. Chen, C. Liu, Y. Fang, X. Ai, F. Zhong, H. Yang, Y. Cao, Understanding of the sodium storage mechanism in hard carbon anodes, Carbon Energy 4 (2022) 1133–1150, https://doi.org/10.1002/cey2.196.

[18] G. Liu, Y. Zhao, K. Deng, Z. Liu, W. Chu, J. Chen, Y. Yang, K. Zheng, H. Huang, W. Ma, L. Song, H. Yang, C. Gu, G. Rao, C. Wang, S. Xie, L. Sun, Highly dense and perfectly aligned single-walled carbon nanotubes fabricated by diamond wire drawing dies, Nano Lett. 8 (2008) 1071–1075, https://doi.org/10.1021/nl073007o.

[19] Y.-R. Rhim, D. Zhang, D.H. Fairbrother, K.A. Wepasnick, K.J. Livi, R.J. Bodnar, D. C. Nagle, Changes in electrical and microstructural properties of microcrystalline cellulose as function of carbonization temperature, Carbon 48 (2010) 1012–1024, https://doi.org/10.1016/j.carbon.2009.11.020.

[20] J.T. Han, J.Y. Cho, J.H. Kim, J.I. Jang, J.S. Kim, H.J. Lee, J.H. Park, J.S. Chae, K. C. Roh, W. Lee, J.Y. Hwang, H.Y. Kim, H.J. Jeong, S.Y. Jeong, G.-W. Lee, Structural recovery of highly oxidized single-walled carbon nanotubes fabricated by kneading and electrochemical applications, Chem. Mater. 31 (2019) 3468–3475, https://doi.org/10.1021/acs.chemmater.9b00719.

[21] A.V. Blokhin, O.V. Voitkevich, G.J. Kabo, Y.U. Paulechka, M.V. Shishonok, A. G. Kabo, V.V. Simirsky, Thermodynamic properties of plant biomass components. Heat capacity, combustion energy, and gasification equilibria of cellulose, J. Chem. Eng. Data 56 (2011) 3523–3531, https://doi.org/10.1021/je200270t.

[22] T. Tohei, A. Kuwabara, F. Oba, I. Tanaka, Debye temperature and stiffness of carbon and boron nitride polymorphs from first principles calculations, Phys. Rev. B 73 (2006) 064304, https://doi.org/10.1103/PhysRevB.73.064304.

[23] J. Hone, B. Batlogg, Z. Benes, M.C. Llaguno, N.M. Nemes, A.T. Johnson, J. E. Fischer, Thermal properties of single-walled carbon nanotubes, MRS Online Proceedings Library (OPL) 633 (2000) 171, https://doi.org/10.1557/PROC-633-A17.1.

[24] M. Antlauf, N. Boulanger, L. Berglund, K. Oksman, O. Andersson, Thermal conductivity of cellulose fibers in different size scales and densities, Biomacromolecules 22 (2021) 3800–3809, https://doi.org/10.1021/acs.biomac.1c00643.

[25] T. Pavlov, L. Vlahovic, D. Staicu, R.J.M. Konings, M.R. Wenman, P. Van Uffelen, R. W. Grimes, A new numerical method and modified apparatus for the simultaneous evaluation of thermo-physical properties above 1500 K: A case study on isostatically pressed graphite, Thermochim. Acta 652 (2017) 39–52, https://doi.org/10.1016/j.tca.2017.03.004.

[26] E. Pop, D. Mann, Q. Wang, K. Goodson, H. Dai, Thermal conductance of an individual single-wall carbon nanotube above room temperature, Nano Lett. 6 (2006) 96–100, https://doi.org/10.1021/nl052145f.

[27] S. Kim, A. Georgiadis, M.M. Tentzeris, Design of inkjet-printed RFID-based sensor on paper: Single- and dual-tag sensor topologies, Sensors 18 (2018) 1958, https://doi.org/10.3390/s18061958.

[28] V. Simone, A. Boulineau, A. de Geyer, D. Rouchon, L. Simonin, S. Martinet, Hard carbon derived from cellulose as anode for sodium ion batteries: Dependence of electrochemical properties on structure, J. Energy Chem. 25 (2016) 761–768, https://doi.org/10.1016/j.jechem.2016.04.016.

[29] D.M. Pozar, Microwave Engineering, 4th ed., John Wiley & Sons Inc, 2011, p. 293.

[30] M. Yu, Y. Han, J. Li, L. Wang, Three-dimensional porous carbon aerogels from sodium carboxymethyl cellulose/poly(vinyl alcohol) composite for high performance supercapacitors, J. Porous Mater. 25 (2018) 1679–1689, https://doi.org/10.1007/s10934-018-0581-8.

[31] T. Meenatchi, V. Priyanka, R. Subadevi, W.-R. Liu, C.-H. Huang, M. Sivakumar, Probe on hard carbon electrode derived from orange peel for energy storage application, Carbon Lett. 31 (2021) 1033–1039, https://doi.org/10.1007/s42823-020-00217-y.

[32] N. Sun, Z. Guan, Y. Liu, Y. Cao, Q. Zhu, H. Liu, Z. Wang, P. Zhang, B. Xu, Extended "adsorption–insertion" model: A new insight into the sodium storage mechanism of hard carbons, Adv. Energy Mater. 9 (2019) 1901351, https://doi.org/10.1002/aenm.201901351.

[33] M.S. Dresselhaus, G. Dresselhaus, A. Jorio, A.G.S. Filho, R. Saito, Raman spectroscopy on isolated single wall carbon nanotubes, Carbon 40 (2002) 2043–2061, https://doi.org/10.1016/S0008-6223(02)00066-0.

[34] J. Rouquerol, D. Avnir, C.W. Fairbridge, D.H. Everett, J.H. Haynes, N. Pernicone, J. D.F. Ramsay, K.S.W. Sing, K.K. Unger, Recommendations for the characterization of porous solids, Pure Appl. Chem. 66 (1994) 1739, https://doi.org/10.1351/pac199466081739.

[35] J. Li, S.J. Kim, S. Han, H. Chae, Characterization of sp^2/sp^3 hybridization ratios of hydrogenated amorphous carbon films deposited in C_2H_2 inductively coupled plasmas, Surf. Coat. Technol. 422 (2021) 127514, https://doi.org/10.1016/j.surfcoat.2021.127514.

[36] D. Xiong, X. Li, Z. Bai, H. Shan, L. Fan, C. Wu, D. Li, S. Lu, Superior cathode performance of nitrogen-doped graphene frameworks for lithium ion batteries, ACS Appl. Mater. Interfaces 9 (2017) 10643–10651, https://doi.org/10.1021/acsami.6b15872.

[37] Y. Su, Y. Liu, P. Liu, D. Wu, X. Zhuang, F. Zhang, X. Feng, Compact coupled graphene and porous polyaryltriazine-derived frameworks as high performance cathodes for lithium-ion batteries, Angew. Chem. Int. Ed. 54 (2015) 1812–1816, https://doi.org/10.1002/anie.201410154.

[38] E. Irisarri, N. Amini, S. Tennison, C.M. Ghimbeu, J. Gorka, C. Vix-Guterl, A. Ponrouch, M.R. Palacin, Optimization of large scale produced hard carbon performance in Na-ion batteries: Effect of precursor, temperature and processing conditions, J. Electrochem. Soc. 165 (2018) A4058–A4066, https://doi.org/10.1149/2.1171816jes.

[39] J.-B. Kim, G.-H. Lee, V.-W.-H. Lau, J. Zhang, F. Zou, M. Chen, L. Zhou, K.-W. Nam, Y.-M. Kang, Microstructural investigation into Na-ion storage behaviors of cellulose-based hard carbons for Na-ion batteries, J. Phys. Chem. C 125 (2021) 14559–14566, https://doi.org/10.1021/acs.jpcc.1c03984.

[40] X.-S. Wu, X.-L. Dong, B.-Y. Wang, J.-L. Xia, W.-C. Li, Revealing the sodium storage behavior of biomass-derived hard carbon by using pure lignin and cellulose as model precursors, Renew. Energy 189 (2022) 630–638, https://doi.org/10.1016/j.renene.2022.03.023.

[41] H. Yamamoto, S. Muratsubaki, K. Kubota, M. Fukunishi, H. Watanabe, J. Kim, S. Komaba, Synthesizing higher-capacity hard-carbons from cellulose for Na- and K-ion batteries, J. Mater. Chem. A 6 (2018) 16844, https://doi.org/10.1039/C8TA05203D.

[42] H. Zhu, F. Shen, W. Luo, S. Zhu, M. Zhao, B. Natarajan, J. Dai, L. Zhou, X. Ji, R. S. Yassar, T. Li, L. Hu, Low temperature carbonization of cellulose nanocrystals for high performance carbon anode of sodium-ion batteries, Nano Energy 33 (2017) 37–44, https://doi.org/10.1016/j.nanoen.2017.01.021.

[43] L. Qin, S. Xu, Z. Lu, L. Wang, L. Chen, D. Zhang, J. Tian, T. Wei, J. Chen, C. Guo, Cellulose as a novel precursor to construct high-performance hard carbon anode toward enhanced sodium-ion batteries, Diam. Relat. Mater. 136 (2023) 110065, https://doi.org/10.1016/j.diamond.2023.110065.

[44] J. Liu, J. Wang, C. Xu, H. Jiang, C. Li, L. Zhang, J. Lin, Z.X. Shen, Advanced energy storage devices: Basic principles, analytical methods, and rational materials design, Adv. Sci. 5 (2018) 1700322, https://doi.org/10.1002/advs.201700322.

[45] W. Yan, J.Y. Kim, W. Xing, K.C. Donavan, T. Ayvazian, R.M. Penner, Lithographically patterned gold/manganese dioxide core/shell nanowires for high capacity, high rate, and high cyclability hybrid electrical energy storage, Chem. Mater. 24 (2012) 2382–2390, https://doi.org/10.1021/cm3011474.

[46] P. Yu, C. Li, X. Guo, Sodium storage and pseudocapacitive charge in textured $Li_4Ti_5O_{12}$ thin films, J. Phys. Chem. C 118 (2014) 10616–10624, https://doi.org/10.1021/jp5010693.

[47] Q. Meng, Y. Lu, F. Ding, Q. Zhang, L. Chen, Y.-S. Hu, Tuning the closed pore structure of hard carbons with the highest Na storage capacity, ACS Energy Lett. 4 (2019) 2608–2612, https://doi.org/10.1021/acsenergylett.9b01900.

[48] L. Yang, M. Hu, H. Zhang, W. Yang, R. Lv, Pore structure regulation of hard carbon: Towards fast and high-capacity sodium-ion storage, J. Colloid and Interface Sci. 566 (2020) 257–264, https://doi.org/10.1016/j.jcis.2020.01.085.

[49] L. Hu, M. Jin, Z. Zhang, H. Chen, F.B. Ajdari, J. Song, Interface-adaptive binder enabled by supramolecular interactions for high-capacity Si/C composite anodes in lithium-ion batteries, 2111560, Adv. Funct. Mater. 32 (2022), https://doi.org/10.1002/adfm.202111560.

[50] P. Stüble, C. Müller, J. Klemens, P. Scharfer, W. Schabel, M. Häringer, J.R. Binder, A. Hofmann, A. Smith, Enabling long-term cycling stability of $Na_3V_2(PO_4)_3$/C vs. hard carbon full-cells, Batter. Supercaps 7 (2024) e202300375.

[51] Y.B. Rao, K.R. Achary, L.N. Patro, Enhanced electrochemical performance of the $Na_3V_2(PO_4)_3$/C cathode material upon doping with Mn/Fe for Na-ion batteries, ACS Omega 7 (2022) 48192–48201, https://doi.org/10.1021/acsomega.2c06261.

[52] Y. Liu, X. Wu, A. Moeez, Z. Peng, Y. Xia, D. Zhao, J. Liu, W. Li, Na-rich $Na_3V_2(PO_4)_3$ cathodes for long cycling rechargeable sodium full cells, Adv. Energy Mater. 13 (2023) 2203283, https://doi.org/10.1002/aenm.202203283.

[53] M. Sharma, R.S. Dhaka, Understanding the electrochemical performance and diffusion kinetics of HC||$Na_3V_2(PO_4)_3$/C full cell battery for energy storage applications, Indian J. Pure Appl. Phy. 62 (2024) 93–101, https://doi.org/10.56042/ijpap.v62i2.7371.

[54] S. Kadam, R. Kate, U. Chothe, P. Chalwadi, J. Shingare, M. Kulkarni, R. Kalubarme, B. Kale, Highly stable MWCNT@NVP composite as a cathode material for Na-ion batteries, ACS Appl. Mater. Interfaces 15 (2023) 34651–34661, https://doi.org/10.1021/acsami.3c02872.